1

Use of the Z Accelerator for Isentropic and Shock Compression Studies

Marcus D. Knudson

1.1 Introduction

The high-pressure equation of state (EOS) of materials is usually determined by shock compression experiments [8,25]. In these experiments a planar, nearly discontinuous pressure wave is generated and allowed to propagate through the material of interest. This steady shock wave is a transition from an initial equilibrium state of pressure, specific volume, and specific internal energy to a final equilibrium thermodynamic state. By considering the conservation of mass, momentum, and energy across the propagating wave front, one can use the kinematic data obtained in these experiments, usually the shock and particle velocity, to determine the pressure–volume–energy states produced by the steady shock wave. Results from several experiments to varying pressure determine the Hugoniot curve, which is the locus of end states attainable through shock compression. The principal Hugoniot curve initiating at standard thermodynamic conditions is a unique path on the EOS surface and is valuable for developing and validating thermodynamic models.

The shock wave technique for probing material at high-pressure is quite mature and has been used for decades to determine the high-pressure response of numerous materials. However, there are many applications where the dynamic loading paths differ significantly from shock loading and are closer to shockless or quasi-isentropic loading. A specific example is the path followed by cryogenic fuels in an inertial confinement experiment to compress hydrogen isotopes to fusion ignition conditions [58]. In other cases, the region of the EOS surface that is of most interest lies well away from the Hugoniot curve. A specific example relates to our understanding of the interiors of the Jovian planets. The inferred structure of the Jovian planets, i.e., whether the planets have a solid core, and if so the size of the core, is quite sensitive to the EOS of hydrogen at several hundred GPa pressures and a few thousand degree temperatures, and provides important clues into the formation process of these giant planets [71]. This region of the EOS surface is much closer to the principal isentrope of hydrogen than the Hugoniot. Finally, Hugoniot and isentropic

compression data complement EOS data acquired by other methods, such as isothermal compression, that together provide a more comprehensive description of the complete EOS [8].

The relationship between these thermodynamic responses is shown in Fig. 1.1. The isotherm represents the pressure–volume response obtained by compressing a material at constant temperature. The cold curve is the isotherm obtained at a temperature of absolute zero, in which the compression behavior is controlled by elastic stresses. The Hugoniot represents an adiabatic compression process by steady shock transitions to various final states, but is highly irreversible, resulting in a higher temperature in the shocked state, and a pressure offset from the isotherm. The isentrope, which lies between the isotherm and the Hugoniot, represents the response obtained for continuous, adiabatic, and reversible compression. In this case there is only a modest temperature increase from the isotherm, resulting in a compression curve that generally lies close to the isotherm. At low pressure where the temperature increase produced by the shock wave is small, the isentrope and the Hugoniot are similar, as illustrated in the figure. It is well known that the isentrope and Hugoniot are second-order tangent at the initial volume state and differ from each other at modest pressures as the third order in volume compression [19].

Dynamic methods can be used to produce shockless, adiabatic loading and obtain dynamic compression data for quasi-isentropic compression. In the case of liquids, dynamic loading on microsecond time scales is continuous, adiabatic, and presumed to be reversible if there are no viscous effects. In the case

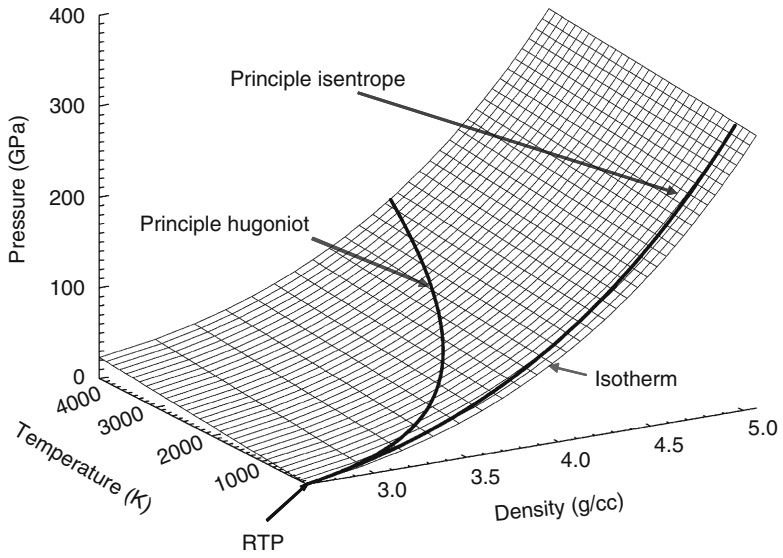

Fig. 1.1. Relationship between the room temperature isotherm, the compression isentrope, and the Hugoniot for aluminum

of solids with rate-independent mechanical response, the loading process is irreversible because of elastic–plastic processes; the longitudinal stress differs from the hydrostatic pressure because of resolved shear stresses that produce an entropy increase from the irreversible work done by deviator stresses. For this reason, ramp loading in solids is usually assumed to be quasi-isentropic although detailed studies are needed on a specific material to determine the extent of departure from isentropic response [29].

Historically several different methods have been utilized in an attempt to generate isentropic compression in solids, with varying degrees of success. These methods include, but are not limited to use of so-called ramp generating materials, such as fused silica and Pyroceram—materials that exhibit anomalous, convex stress–strain behavior over a limited stress range (below $\sim$3 and $\sim$20 GPa for fused silica and Pyroceram, respectively) [12, 17]; high velocity impact with graded density impactors [11, 63, 64]; cylindrically converging magnetic compression [40]; and a plasma piston concept using either laser deposition or high explosives to generate an expanding plasma that stagnates on a sample of interest [15, 31, 55, 68, 69]. These methods will not be discussed here. However, it is noted that many of these methods achieved limited success, mainly due to the difficulty in producing smooth, repeatable ramp compression for use in high-fidelity isentropic compression experiments.

This article will focus on recently developed techniques using magnetic loading on the Sandia Z accelerator to both significantly improve the smoothness of the ramp load introduced into a planar specimen, and also to extend the pressure range accessible with smooth ramp loading. This breakthrough in capability has resulted in several recent publications [6,10,35,36,38,66]. It has also been recognized that the magnetic loading achievable on the Z accelerator is very well-suited for acceleration of flyer plates to ultrahigh velocity [37, 51]. In particular, the timescales and peak accelerations achievable on Z are such that velocities exceeding 30 km/s are attainable. Furthermore, the exceptionally smooth and uniform pressure pulse enables intact, high integrity plates to be launched in spite of the extreme accelerations (of order 10^{10}g). In fact, flyer plate velocities as high as $32\,\mathrm{km\,s^{-1}}$ have been measured in which the condition of the plate at impact is essentially ambient temperature and density [47]. These developments in isentropic compression experiments (ICE) and high velocity flyer plate shock wave experiments on the Z accelerated will be discussed in the following sections.

1.2 Experimental Technique

1.2.1 ICE Experimental Configuration

The Z accelerator [59] is a low inductance pulsed power generator capable of capacitively storing 11.6 MJ of electrical energy. In the ICE configuration the machine utilizes a combination of fast switches and transmission lines to

deliver a ∼20 MA, ∼300 ns rise-time current pulse to a short circuit load at the center of the accelerator. This pulse generates a time-varying magnetic field between the anode and cathode of the short circuit. As a result of the Lorentz force, these high currents and magnetic fields produce quasi-isentropic compression of the cathode and anode over the discharge time of the accelerator [6]. Fields of the order several MG are produced, which result in magnetic pressure levels approaching 400 GPa.

With the aid of accurate magneto-hydrodynamic (MHD) simulations, which will be described later, short circuit loads have been designed that are capable of generating planar stress waves in centimeter sized material samples. The experimental configuration is shown schematically in Fig. 1.2. Typically, four anode panels are arranged about a central stainless steel or tungsten cathode post, forming a symmetric anode–cathode (A–K) gap. A short circuit is created between the anode panels and the cathode post through a shorting cap at the top of the coaxial load. The interaction of the current density and magnetic field produced in the insulating gap results in a time-dependent pressure, $P(t)$, that is applied to the inner surface of the electrodes. The magnitude of this loading is given by

$$P(t) = B^2(t)/2\mu_0 = \mu_0 J^2(t)/2 = \mu_0 I^2(t)/2S^2. \tag{1.1}$$

Here, $I(t)$ is time-dependent current at the sample location; S is the scale length necessary to convert $I(t)$ to the current density, $J(t)$ (amps/unit length); $B(t)$ is the corresponding magnetic field strength; and μ_0 is the magnetic permeability of free space. The scale length S is typically between 2 and 10 cm, and is both load geometry dependent and time dependent, and will be

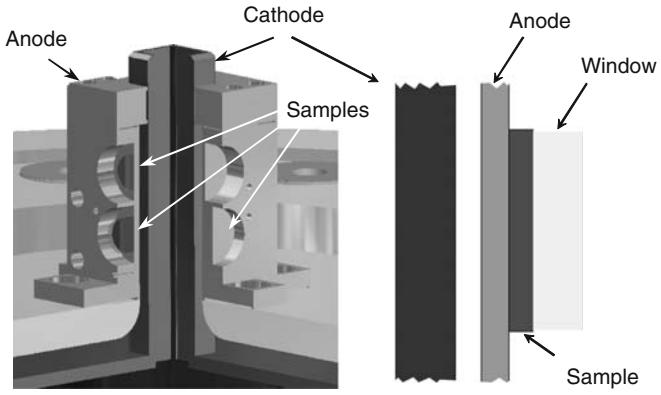

Fig. 1.2. Experimental configuration for isentropic loading on Z, in this case the square short circuit geometry. The square cathode and flat plate anode produce a planar magnetic field within the A–K gap. The sample of interest (which may be backed by a window) is mounted onto the anode plate. The typical dimension of the short circuit load is ∼20 to 35 mm square (outside dimension of the cathode) by ∼30 to 50 mm in height

discussed further below. The magnetic pressure applied to the anode surface induces a hydrodynamic stress wave of equal magnitude and rise-time that propagates into the anode material.

Each anode panel becomes an experimental platform with the capability of accommodating several samples that are all subjected to essentially identical loading. 2-D MHD calculations have been performed for this configuration and show that magnetic field uniformity of about 0.5% can be obtained over the central horizontal region of the anode plate [66]. In addition, these calculations indicate considerably better uniformity along the entire length of the coaxial load. In this way up to five samples can be stacked vertically on a panel, within the planar loading region, and as many as twenty samples can be subjected simultaneously to identical, planar loading histories in a single firing of the accelerator.

The magnitude of the peak magnetic field in the A–K gap, thus the peak magnetic pressure, can be adjusted by changing the geometry of the short circuit load, and therefore the current density. Two typical short circuit geometries are routinely used in materials testing: a square coaxial geometry, in which four anode panels of equal width surround a square cathode stalk, and a rectangular geometry, in which two sides of the square geometry are reduced to roughly half the width. The square geometry produces magnetic pressures up to ∼100 GPa. The rectangular or slab geometry produces up to ∼300 to 400 GPa of magnetic pressure through increased current density, but at the expense of available sample area. In addition to varying the short circuit geometry, the current density for a given geometry can also be lowered by reducing the charge voltage of the accelerator. Since the peak current scales approximately linearly with the charge voltage, the magnetic pressure can be reduced by as much as ∼45% using this approach. These two parameters, the geometry and the charge voltage, allow the peak magnetic pressure to be continuously varied from a few tenths of a GPa to several hundreds of GPa.

1.2.2 MHD Modeling

Due to significant joule heating and resulting ablation of the conducting plate near the current carrying surface, as well as magnetic field penetration into the metal associated with this technique, the specific details of ramp loading are extremely complicated [56]. The magnetic loading process in depicted schematically in Fig. 1.3, which shows a cross section of the anode cathode gap in the plane of current flow on one side of a coaxial short circuit load on Z. The current flowing at the anode and cathode surface induces a magnetic field in the A–K gap, and the resulting Lorentz force is transferred to the electrode material, propagating a ramp compression wave into the sample. As material on the surface is Joule heated, the conductivity drops precipitously, and current begins to diffuse into the electrode material, resulting in a magnetic diffusion front that trails behind the stress wave front. Thus at any given time a snapshot of the sample material can be divided into three

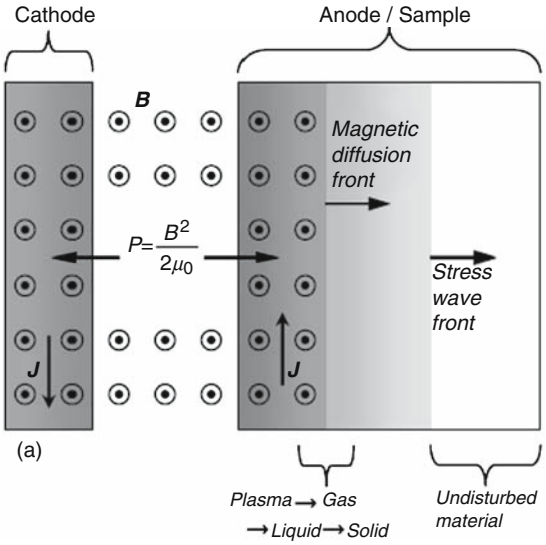

Fig. 1.3. Schematic virtual cross section of one side of an ICE load on Z. Indicated in the figure are the directions of the magnetic field, B, and current, J, as well as relative positions of the propagating magnetic diffusion and stress wave fronts

regions, which from right to left in the figure are (a) a region of undisturbed material in front of the advancing stress wave, (b) a region of material that has been processed by dynamic compression, but has not yet been affected by the advancing magnetic diffusion front, and (c) a region of material that has been processed by magnetic diffusion and consists of anode material heated from solid to liquid, gas, and plasma states.

Computer simulations, which include all the experimental parameters and the necessary physical properties of the conducting plate, are of great value in designing the experimental configuration. This is particularly true for high-pressure ICE experiments; in addition to the complex physics associated with the Joule heating and field diffusion, there is significant deformation of the anode and cathode plates during the rise-time of the current pulse. This deformation results in significant increases in load region inductance with time, which affects the shape of the current rise as well as the maximum current achieved. Furthermore, the load deformation alters the scale length, S, used in converting current to magnetic field strength, and thus to magnetic pressure acting on the anode. This further modifies the shape and peak of the resulting pressure pulse obtained from the current pulse.

In order to achieve a predictive modeling capability to help guide the design and optimization of the experimental configuration, both 1-D and 2-D Eulerian simulation platforms have been developed using the finite element, arbitrary Lagrangian–Eulerian, MHD code ALEGRA [75] to solve the MHD equations for a compressible material with material strength.

In these simulations, a complete equation of state valid for a wide range of pressures, densities, and temperatures is used for the conductor materials, in addition to physical models for thermal and electrical conductivities [26, 28]. Material density and internal energy are used in the EOS to obtain pressure and temperature at each time step in the calculation. The calculated density and temperature are used in the conductivity model to obtain electrical and thermal conductivities. More details concerning the MHD modeling can be found elsewhere [56, 57].

Results of 1-D MHD simulations, using experimentally measured current profiles at the load region as the input, are in very good agreement with experiment and have provided significant insight into the details of the magnetic loading [56]. As an example, snapshots at two different times from a 1-D MHD simulation are shown in Fig. 1.4. These snapshots nicely illustrate the physics involved in the magnetically driven ICE experiment. In particular, note the time evolution of the hydrodynamic pressure wave, the magnetic diffusion front, and the material density profile. Several points are evident. First, there is significant diffusion of the current and field into the electrode during the timescale of the experiment; the location of the current, the shaded region in the figure, is bounded on the left by the density profile (the current must reside in the anode material) and on the right by the magnetic pressure profile. However, the predictions of the magnetic diffusion rates, of order 2–3 $\mathrm{km\,s^{-1}}$ depending on the current density, are significantly lower than the wave speeds of the hydrodynamic front. This is significant since the stress waves, which typically propagate at speeds of ∼4 to 7 $\mathrm{km\,s^{-1}}$, outrun the lagging diffusion wave. This ensures that the hydrodynamic wave propagation occurs in virgin material that has not been affected by magnetic field effects and Joule heating. The predicted diffusion rates are in good agreement with experimental results [56, 73]. Second, note that there is not a well-defined boundary at which the magnetic pressure is applied; the pressure emanates from the entire Joule heated region. Furthermore, this region both broadens with time and propagates into the electrode. This is significant since wave interactions emanating from either a free surface or window interface will interact with this rather ill-defined pressure boundary earlier than would be expected had the pressure boundary been confined to the initial power-flow surface. Careful attention to this effect is required when designing ICE experiments, as will be discussed in Sect. 1.4.1.

Two-dimensional MHD simulations enable determination of the extent of pressure gradients due to magnetic field gradients within the A–K gap, as well as the effect of load deformation on the resulting current pulse. The 2-D nature of the square or rectangular short circuit load results in magnetic pressure gradients across the horizontal direction of the anode plate (perpendicular to the axis of the load). The electromagnetic (EM) code QUICKSILVER [72] was used to determine these gradients for the initial geometry of the anode and cathode. As a specific example, the simulations indicate that magnetic pressure is uniform to better than 1% over the central 6 mm of a 15-mm wide anode

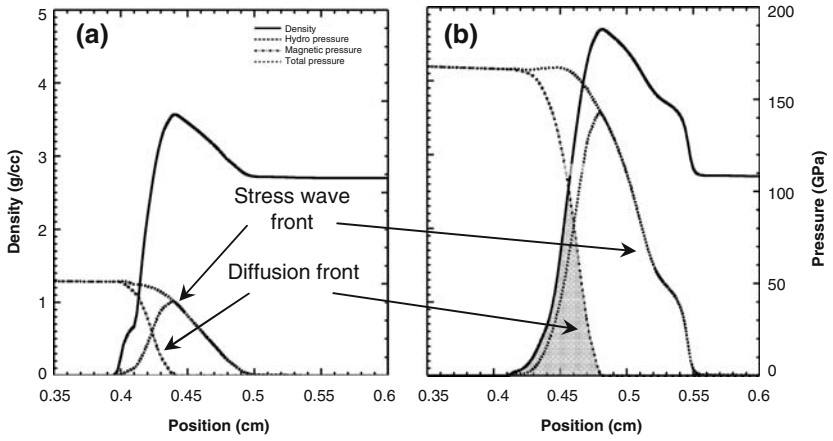

Fig. 1.4. Snapshots of a 1-D MHD calculation at two different times (2.46 and 2.56 μs) during loading; in this case an ICE experiment on aluminum to ∼170 GPa. Indicated in the figure are the density profile, and the hydrodynamic, magnetic, and total pressure. The region of current flow is denoted by the shaded region bounded on the left and right by the density and magnetic pressure profiles, respectively

plate. However, the applied pressure drops quite rapidly toward the corners of the cathode due to magnetic field gradients that cause slight hydrodynamic pressure variations across the anode surface. The pressure variations result in an unequal expansion of the A–K gap, which, independent of additional edge effects, gives rise to further pressure gradients across the anode. Consequently, the area over which the magnetic pressure is uniform decreases as a function of time. Nevertheless, 2-D MHD simulations that account for the time-dependent deformation of the A–K gap suggest that the central ∼4 to 5 mm width of the original 15-mm wide anode remains at a nearly uniform pressure to late times [57]. These numerical simulations were confirmed with a line imaging VISAR diagnostic [76] that measures spatially resolved particle velocity [36].

In contrast, the magnetic pressure gradient is rather independent of height along the coaxial short circuit load. There are variations as a function of height near the transition of the cathode from a radial feed to a coaxial feed. However, the current density is quickly redistributed and becomes substantially uniform over the coaxial region of interest. This suggests there should be little to no gradient along the vertical direction; i.e., the principal gradients are limited to the horizontal direction. This has also been verified experimentally using a line imaging VISAR diagnostic [36].

As mentioned above, power flow into the ICE load is affected by the dynamics of the electrodes caused by the magnetic pressure. Deformation of the load conductors, material motion, and Joule heating all result in an increase in the inductance and resistance of the load during the current pulse.

Simulations must account for the coupling between the accelerator and the load in a self-consistent manner in order to accurately predict the drive current and the time-dependent loading profile of the stress wave. This is accomplished by coupling an accurate circuit model of the accelerator to the 2-D simulation of the load [57].

The specific circuit, shown in Fig. 1.5, includes equivalent resistances and inductances for the accelerator, as well as a time-dependent model of current loss and a time-dependent resistance that emulates a short circuit, both of which occur upstream of the MHD load. Values for the inductances L_{m}, $L_{\mathrm{convolute}}$, and L_{im} are determined from geometrical considerations. The inductance of the MHD load is calculated self-consistently in the simulation using an effective transverse length representative of the actual experimental load. The circuit is driven by a time-dependent accelerator voltage obtained from experimental measurements of accelerator performance in which similar short circuit loads were used.

2-D simulations using such a circuit model produce upstream currents (load current) and downstream currents (current in the magnetically insulated transmission lines (mitl) the feed lines inside the vacuum section of the accelerator), denoted I_{u} and I_{d}, respectively, that accurately match the experimentally measured values, as shown in Fig. 1.6. It is the load current, I_{d}, along with the time-varying scale length, S, that effectively determines the shape of the pressure pulse that drives the ICE load. These MHD simulations are invaluable for providing an accurate means to predict peak pressures and

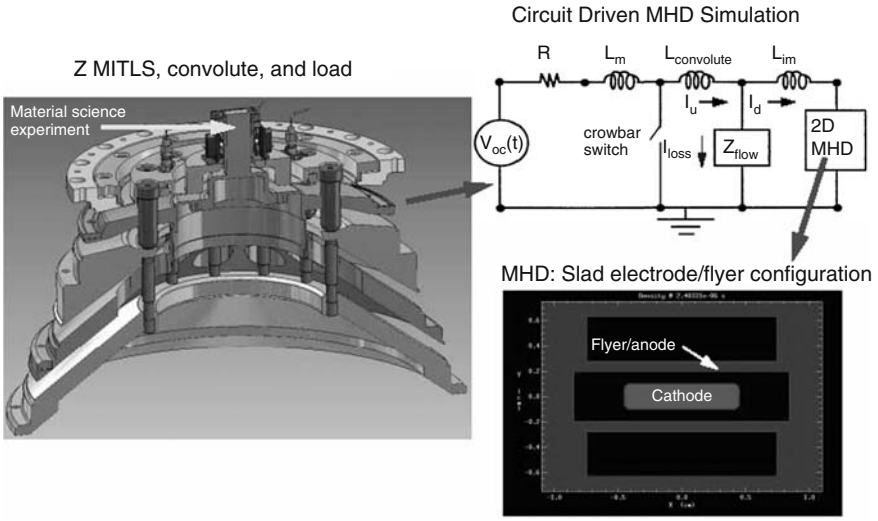

Fig. 1.5. Convolute section (left) and circuit model of the Z accelerator with a 2-D simulation as one of the circuit elements (right). In this case, the 2-D simulation is of a rectangular geometry short circuit load

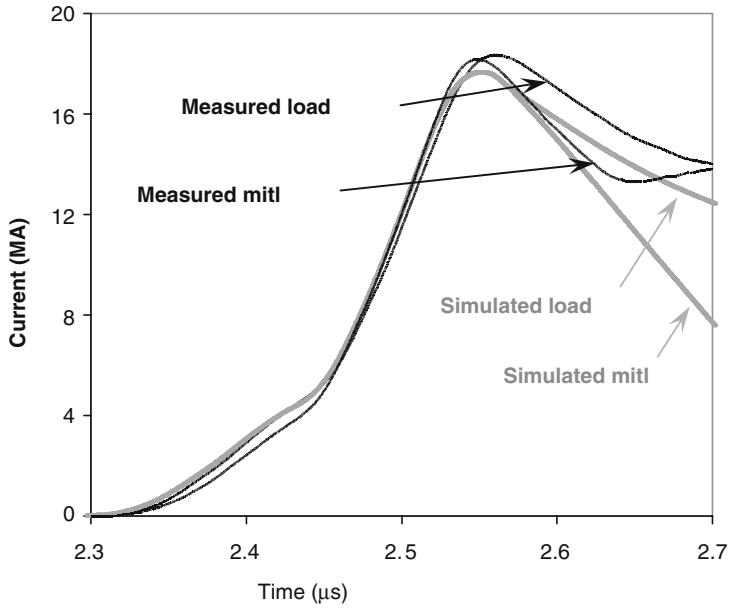

Fig. 1.6. Comparison of simulated (gray) and measured (black) load current and magnetically insulated transmission line (mitl) current. Measurement accurate to ∼5% to 10%

magnetic diffusion for arbitrary short circuit configurations and are critical for designing ICE experiments. This recent advance in the ability to predict the performance of arbitrary load geometries from known input conditions and material properties has allowed the identification of optimal anode and cathode geometries, which have resulted in peak stresses of nearly 400 GPa applied to planar samples.

1.2.3 Pulse Shaping

In the normal firing configuration of the Z accelerator, all 36 individual transmission lines are triggered simultaneously through laser initiated gas-switches. This firing configuration results in essentially a linearly increasing current pulse with a rise-time of ∼200 ns. In most materials, the ensuing ramp wave will tend to form a shock at the base of the wave after propagation of only a few hundred microns (see Fig 1.9b). It is possible to substantially increase the propagation distance without shock formation by tailoring the current pulse.

Wave propagation in a material is governed by its dynamic properties. In most materials the local sound speed increases with increasing pressure. This is illustrated conceptually in Fig. 1.1, which shows a convex isentrope and Hugoniot in the P–V plane. Thus the ramp wave tends to steepen as it propagates into the sample, as illustrated in Fig. 1.7a. If the propagation distance

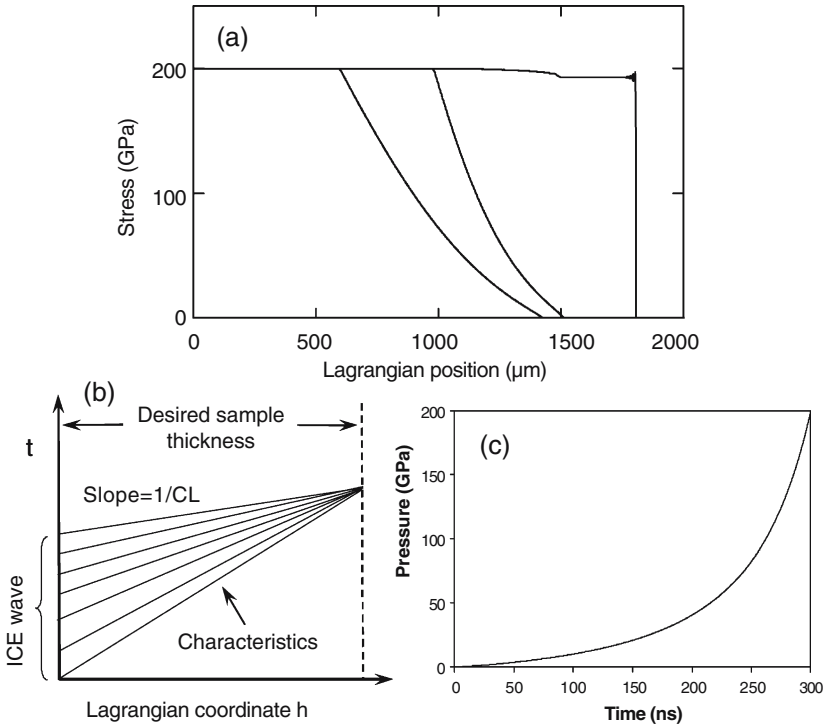

Fig. 1.7. (**a**) Evolution of an ideal ramp profile in aluminum; shock formation occurs abruptly at a single location and time in the specimen, near 1.8 mm. (**b**) x–t diagram showing characteristics emanating from a 300 ns tailored ramp. (**c**) Ideal pressure profile for a 200 GPa ramp wave in aluminum with a 300 ns rise-time

is sufficiently long, the wave will eventually evolve into a steady, nearly discontinuous jump in pressure, density, energy, temperature, and entropy; this wave is referred to as a steady shock wave, as discussed earlier.

In the idealized optimal case, the ramp will abruptly form a single, high-amplitude shock at a specific location in the specimen. At this point, the isentropic pressure will generally drop precipitously from the drive pressure to a state on the Hugoniot for the material; a rarefaction fan is observed to propagate back into the compressed material and a shock is formed that propagates to the right. Such an ideal profile maximizes the propagation distance for a given rise-time prior to shock formation. If the approximate P–ρ isentrope of a material is known, the ideal profile can be estimated by mapping the material $P(C_L)$ curve onto a $P(t)$ curve using a position–time diagram, as illustrated in Fig. 1.7b. It is desired that all of the characteristics converge at a single time and position in the sample. Projecting these characteristics, which have a slope given by the inverse of the Lagrangian wave speed at the particular pressure, backwards in both space and time to a given location in

the sample results in the desired optimal $P(t)$ profile. Note that the rise-time of the resulting pulse depends upon the desired thickness of the sample; i.e., a longer rise-time is required to delay shock formation for propagation through a thicker sample. As an example, the optimal pressure profile determined in this way for a 200 GPa ramp wave in aluminum is shown in Fig. 1.7c. In this case the rise-time is 300 ns, and the shockless propagation distance is ∼1.8 mm. For completeness, we note there are slight modifications necessary to account for MHD effects and the significant deformation of the load. Nevertheless, this profile accurately represents the form of the required current pulse.

Current tailoring, or pulse shaping, is required to reproduce the desired current shape. The shape of the overall pulse delivered to the load is controlled by staggering the gas-switch laser trigger times of the 36 transmission lines. The staggered pulses mix together in four radial mitl's, each fed by nine lines. The mitl's cross through an insulator stack into the vacuum section of Z, then mix into a single feed gap at the convolute section shown in Fig. 1.5. The mitl levels are shown in cross-section, labeled A–D, in Fig. 1.8a.

The staggering of the lines is done within nine timing groups of four transmission lines each, with each group spanning all four mitl's at a common azimuth. This is done to maintain level-to-level symmetry, and avoid current reversal and subsequent arcing at the vacuum stack which has been observed when using other pulse shaping schemes that placed emphasis on 3-point current symmetry within each level, at the expense of level-to-level symmetry. The distribution of firing times in azimuthal position around the machine is found by computing the time-angle moment for all possible permutations of the firing order; the minimum moment gives the minimum asymmetry in current flow. The technique, which is analogous to tightening the lug nuts on a wheel, is depicted graphically in Fig. 1.8b.

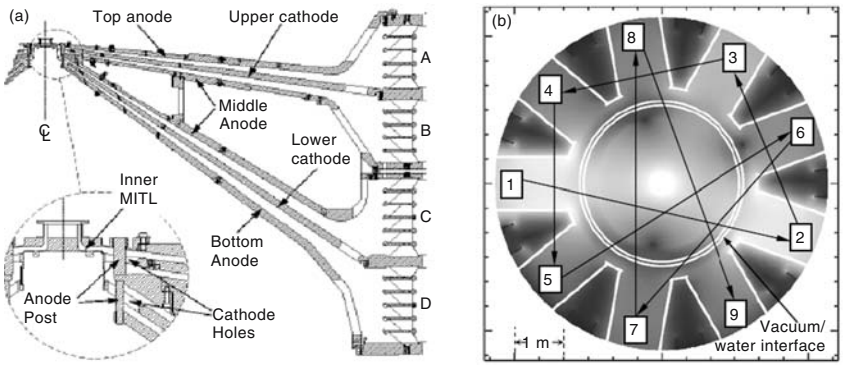

Fig. 1.8. (**a**) Side section view of the center vacuum section of the Z accelerator showing the four mitl levels A–D. (**b**) Top view of a single mitl level showing magnetic field contours from a 3-D electromagnetic calculation with staggered timing of nine module groups; numbers and arrows indicate the firing order

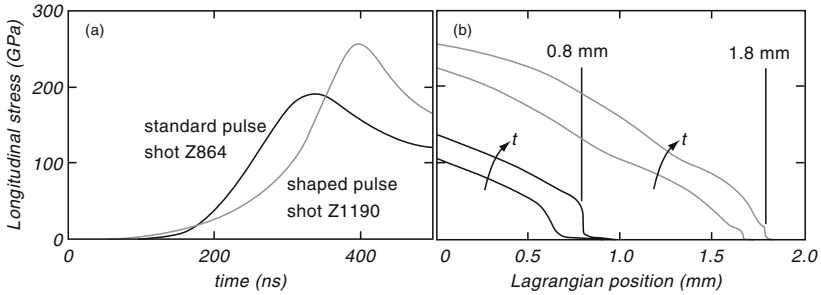

Fig. 1.9. (**a**) Effective stress boundary conditions for a standard (unshaped) pulse (black) and a typical shaped pulse (gray); the difference in the peak stress is due to a difference in load geometry. (**b**) Calculated snapshots of longitudinal stress at two times for each pulse; a shock initially forms at a Lagrangian position of 0.8 and 1.8 mm for the unshaped and shaped pulses, respectively

This modification to the accelerator enables significant flexibility and allows nearly arbitrary current profiles to be produced. Pulse shaping has enabled a more concave current profile to be produced, which is necessary to delay shock formation to a few millimeters propagation distance for most materials. In particular, Fig. 1.9 shows snapshots of Lagrangian stress at two different times for aluminum isentropically compressed with a typical unshaped (black) and shaped (gray) pulse. The advent of pulse shaping in this case increases the shockless propagation distance from ∼800 to ∼1800 μm. This type of pulse shaping control was critical in performing many of the experiments that are described in Sect. 1.4.

1.2.4 Magnetically Accelerated Flyer Plates

In the magnetically accelerated flyer plate technique, the interaction of the current density and magnetic field produced in the insulating gap results in an impulsive ramp load, providing momentum to the anode, launching it as an effective flyer plate to high velocity. The flyer plate configuration is shown schematically in Fig. 1.10. Each anode panel becomes a flyer plate; this is achieved by machining the entire current carrying portion of the aluminum anode panel to a prescribed material thickness of approximately 800–900 μm. To retain rigidity, and to allow the panels to be assembled together, this flyer frame is attached to a panel back as shown in Fig. 1.10b. The panel back also allows for mounting of the experimental targets at a prescribed distance from the flyer plate, which is typically ∼3 to 4 mm, and the mounting of optical probes used to diagnose the targets. Each of the panel backs can hold several separate targets, allowing multiple, simultaneous shock wave experiments during a single firing of the accelerator.

Again, computer simulations, which include all the experimental parameters and necessary physics, are of great value in designing the experimental

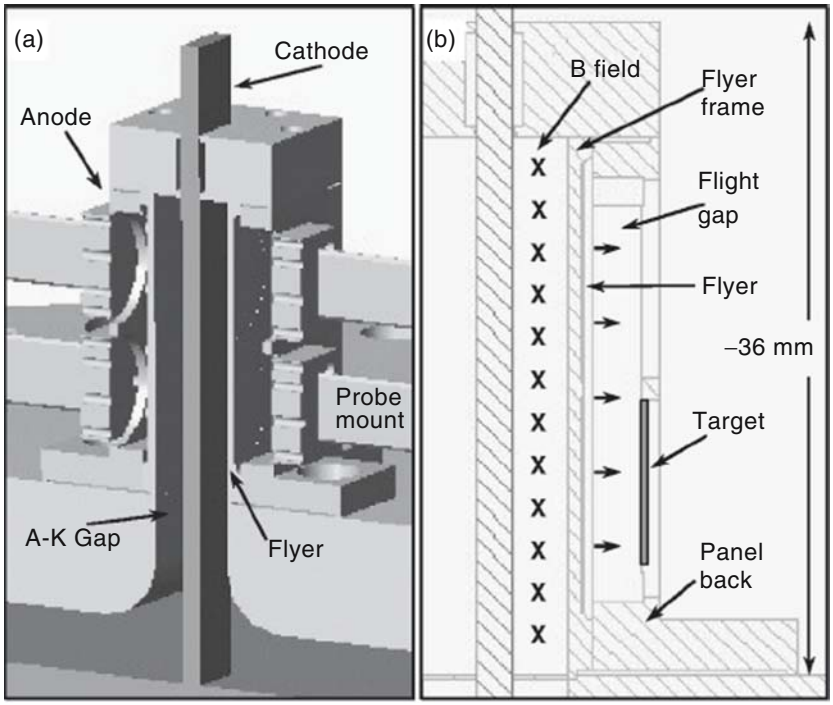

Fig. 1.10. Schematic of the load used to launch flyer plates on the Z accelerator, in this case the rectangular short circuit geometry. (**a**) Section view of the coaxial load. Also shown are the probe mounts used to hold the fiber optics used to diagnose the sample. (**b**) Section view showing more detail

configuration that minimizes density gradients in the flyer plate at impact and accurately predicts the final flyer plate velocity and optimal flight distance [56, 57]. The same circuit model as described above is used. In developing the self-consistent, 2-D modeling capability for these high-velocity flyer plate experiments, it was determined necessary to invoke a time dependent loss and crowbar model that emulates a short circuit at the convolute of the accelerator. Evidently, due to the presence of magnetic nulls in the complex geometry of the convolute section (see Fig. 1.5), there is significant electron loss to the anode. Electron bombardment of the anode creates a plasma which eventually results in shorting of the A–K gap at a time just after peak current. The effect of this current loss and short circuit is twofold. First, the peak load current, I_{d}, is reduced somewhat due to the current loss upstream of the load. Second, after the short circuit occurs, flux is trapped downstream of the short, and the current subsequently decays with a time constant indicative of the inductance downstream of the short. This tends to result in a slower decay of the load current relative to the mitl current. Indeed this phenomenon is

predicted in the 2-D simulations, as illustrated in Fig. 1.6. This slower decay of the load current is necessary to reproduce the magnitude of the reverberation in the flyer plate velocity profile observed experimentally. Thus, both experiment and simulation indicate the presence of a machine-dependent loss impedance and short circuiting.

Figure 1.11 shows a comparison between the predicted flyer velocity and the actual measured flyer velocity for a $\sim$28 km s^{-1} launch. The agreement between simulation and experiment over the entire trajectory indicates that several key details concerning the launch of the flyer plate are accurately reproduced in the simulations. In particular, the two portions of the flyer trajectory highlighted in Fig. 1.11 provide a good indication as to the peak current at the load, the magnitude of the current slightly beyond the peak, and the extent of magnetic diffusion and associated Joule heating. The initial velocity increase (black line protion), over the first $\sim$75–100 ns of the launch, is the result of the driving pressure pulse reaching the free surface (impact surface) of the flyer plate. This wave interaction results in acceleration of the free surface and the propagation of a rarefaction wave back into the flyer plate. Thus, the peak velocity at the end of this stage of the launch provides a measure of the magnitude of the driving pressure pulse, and therefore the magnitude of the peak current at the load. Somewhat later in time the rarefaction reaches the portion of the flyer plate in which the majority of the current is flowing. This region is a few hundred μm into the flyer plate due to magnetic diffusion. The interaction of the rarefaction with the magnetic pressure results in a recompression wave that propagates back toward the free surface of the flyer. The magnitude of the magnetic pressure at the time of this interaction, which relates to the magnitude of the

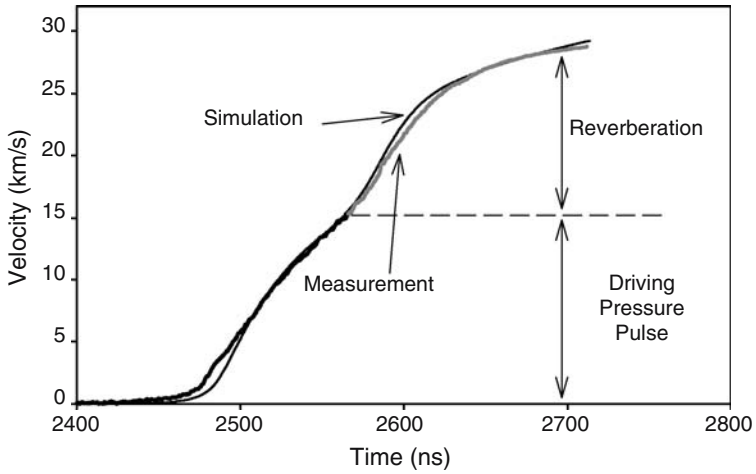

Fig. 1.11. Comparison of the simulated and measured flyer velocity profile for an aluminum plate launched to $\sim$28 km s^{-1}

current at that time, dictates the magnitude of this recompression. When the recompression reaches the free surface, the free surface is again accelerated, and the flyer plate receives a second impulse driving it to higher velocity (gray line portion). Thus, the magnitude of the second increase in velocity provides a measure of the current at the load just beyond peak current. Finally, the extent of magnetic diffusion and Joule heating can be inferred from the sharpness of the reverberation. If there were very little diffusion and Joule heating, there would be a relatively sharp density gradient at the power-flow side of the flyer plate, and the reverberation would be quite pronounced. In contrast, if there were significant diffusion and Joule heating, the density gradient would be quite broad, and the resulting reverberation would also be broad and difficult to identify. The level of agreement in the form of the reverberation between simulation and experiment in Fig. 1.11 indicates that the extent of diffusion and Joule heating is well reproduced in the simulations.

Using this simulation capability various load configurations have been explored in order to identify the optimal load geometry to launch high-velocity flyer plates that are suitable for use in EOS experiments. The final symmetric rectangular design that is routinely used to launch flyer plates to these high velocities ($\sim$23 to 28 km s^{-1}) is shown in Fig. 1.12. The nominal cathode outer dimensions are 9 mm wide by X mm thick (where $X = 4, 2$, or 1), and the nominal anode inner dimensions are 17 mm by $X + 2$ mm. Thus, the A–K gaps are 4 mm on the unused sides of the coaxial load and 1 mm on the flyer plate sides of the load. The thickness of the cathode is determined by the desired velocity of the flyer; 4, 2, and 1 mm cathodes result in approximately 23, 26, and 28 km/s aluminum flyer plate velocities, respectively.

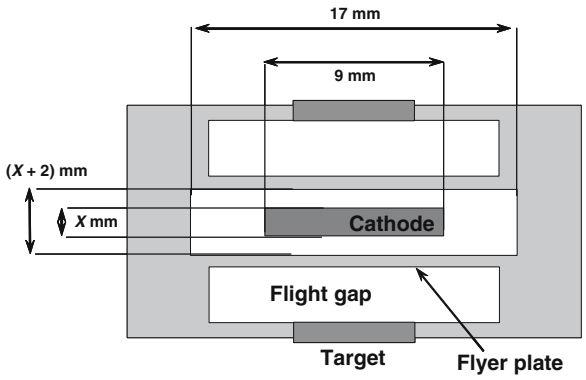

Fig. 1.12. Top view of the optimal load geometry used to launch flyer plates to velocities up to 28 km s^{-1} on the Z accelerator

The velocity dependence on cathode thickness, with all other dimensions the same, can be understood by the fact that a thinner cathode corresponds to a lower overall current carrying surface on the anode, and a lower overall inductance. Both of these characteristics result in a larger driving pressure, and therefore a higher flyer plate velocity. The optimization of the cathode width is a compromise between the current density and 2-D effects resulting in flyer plate deformation. Clearly, a larger current density is achievable with a smaller cathode width. However, flyer plate deformation is also magnified with a smaller cathode width. The 2-D nature of the short circuit load results in magnetic pressure gradients across the horizontal direction of the flyer plate (perpendicular to the axis of the load). These gradients cause velocity variations across the flyer surface, leading to nonuniform increase in the A–K gap that increases as the flyer is launched toward the target. Consequently, the area over which the magnetic pressure is uniform is reduced. Nevertheless, 2-D MHD simulations that account for the time-dependent deformation of the A–K gap [57] suggest that the central ∼3 to 4 mm width remains largely planar at impact for a configuration with a 9-mm-wide cathode. As in the case of the ICE configuration, the uniformity along the length of the coaxial load is quite good. This provides a region ∼3 to 4 mm in width along the entire height of the load for performing planar shock wave experiments.

The highest velocities that have been obtained to date, namely $\sim 32\,\mathrm{km\,s^{-1}}$, were obtained using an asymmetric load geometry. The geometry is similar to that shown in Fig. 1.12 but with the upper A–K gap extended from 1 to 13 mm; the inner anode box dimension is 17×15 mm and the cathode is 9×1 mm with a 1 mm A–K gap between the cathode and the lone flyer plate. The resulting inductance imbalance between the four sides of the anode box (A–K gaps of 1, 4, 13, and 4 mm going around the load starting at the bottom) causes the vast majority of the current to preferentially flow along the lower 1 mm A–K gap. This results in a significant increase to the momentum imparted to the flyer plate, and ∼10% increase in the peak flyer velocity, at the expense of available sample area. Due to the nonlinearity in shock impedance at these high pressures, ∼10% increase in flyer velocity results in ∼20% increase in impact pressure, which significantly increases the pressures achievable in high velocity flyer plate experiments.

1.3 Analysis Techniques

The governing equations for planar shock or ramp loading are summarized as follows for a solid initially at rest [1, 8, 25]. For a shock wave, we have

$$\sigma - \sigma_0 = \rho_0 \, U_\mathrm{s} \, u_\mathrm{p}, \tag{1.2}$$

$$V/V_0 = 1 - (u_\mathrm{p}/U_\mathrm{s}), \tag{1.3}$$

$$E - E_0 = \tfrac{1}{2}(\sigma - \sigma_0)(V_0 - V), \tag{1.4}$$

and for a ramp wave we have

$$\mathrm{d}\sigma = \rho_0 \, C_\mathrm{L} \, \mathrm{d}u_\mathrm{p}, \tag{1.5}$$

$$\mathrm{d}\sigma = \rho_0 \, C_\mathrm{L} \, \mathrm{d}u_\mathrm{p}, \tag{1.6}$$

$$\mathrm{d}E = -\sigma(S_0) \, \mathrm{d}V. \tag{1.7}$$

Here, σ is longitudinal stress; ρ is density; U_s is shock velocity; u_p is particle velocity; V is specific volume $(1/\rho)$; E is specific internal energy; C_L is Lagrangian sound speed; and S is entropy. Zero subscripts refer to the initial state. In the case of ramp compression we have made the assumption of simple waves where there is no rate dependence and the flow is isentropic $(S = S_0 = \text{constant})$.

Measurement of any two of the shock variables in (1.2)–(1.4) allows determination of all five quantities. The locus of end states produced by steady shock compression defines the Hugoniot curve illustrated schematically in Fig. 1.1. In the Z flyer plate experiments, typically the shock velocity and particle velocity are measured using fiber optic based diagnostics. The shock velocity is obtained through the use of a fiber optic shock break out (FOSBO) technique, which is sensitive to the sudden change in reflectivity upon emergence of a strong shock. The transit times through typical sample thickness of $\sim$300/900 µm are of order 15–40 ns, resulting in accuracy in the inferred shock velocity of $\sim$1–3%. The particle velocity is obtained by directly measuring the flyer velocity using the velocity interferometer system for any reflector (VISAR) technique, originally developed by [13]. In symmetric impact experiments, where the impacting plate and the sample are identical, the projectile velocity is exactly one half of the projectile velocity. In other cases, the impedance matching technique must be used to infer the particle velocity of the sample of interest. In either case, the particle velocity can be inferred quite accurately, typically to within $\sim$1% to 2%. Examples of the use of Z in flyer plate Hugoniot experiments will be given in Sect. 1.4.4.

In ramp wave experiments, it is also necessary to measure two variables for the complete ramp loading history. This is typically accomplished by measuring the velocity profile of either a free or windowed surface for at least two different specimen thicknesses. The histories of ramp compression at various sample thicknesses must be precisely measured because of the short transit times obtained from the necessarily small samples in magnetic loading experiments (usually of order 0.5–1 mm). Typically, the particle velocity must be measured to $\sim$1% or better, and the relative timing of wave profiles for the various sample thicknesses to within $\sim$0.5 ns, in order to achieve accuracies in the order of 2–3% in stress and comparable accuracies in density from experimental records in the pressure range below $\sim$100 GPa. Velocity interferometry is one of the most useful techniques for measuring wave profiles at high stresses because of the high precision in particle velocity and the high time-resolution that can be achieved, and has been employed in all of the ICE experiments discussed in Sect. 1.4.

Lagrangian and Backward Analysis Techniques

The dynamic isentropic material response can be determined from measured interface velocities using (1.5)–(1.7). However, the analysis of these wave profiles is not straightforward. Ideally, in situ wave profile measurements are needed to determine accurate wave velocities in order to implement the Lagrangian wave analysis technique. This is difficult to achieve while maintaining high time-resolution, so the method has not yet been applied to ramp loading experiments with the Z Accelerator. Optical windows can be used in velocity interferometer experiments to achieve the required time-resolution, but the impedance mismatch between a specimen and window results in wave reflections and interactions that perturb the ramp wave. This causes the measured profile to be considerably different than the profile that a true in situ gauge would record. Nevertheless, given the velocity profiles for at least two sample thicknesses subjected to ramp wave loading, the general equations of motion in (1.5), (1.6), and (1.7) can be applied, assuming simple waves [1, 36, 66].

For cases where the yield stress is negligible compared to the peak stress and the waves are shown to be self-similar (simple), Hayes has developed a numerical integration technique that is particularly useful [41]. This method uses the measured wave profiles at two or more sample thicknesses, either from a free surface or a sample/window interface measurement, and a "backward" integration of the equations of motion to determine the stress–time profile at a specified location within the sample. The wave profile provides an initial condition of velocity, stress, and density at the Lagrangian position of the measurement, and a finite-difference method is used to integrate the equations of motion in the negative spatial dimension assuming a stress–volume response for the material. This provides a stress profile at a location within the sample that is free of interaction effects over the time of interest. By iteratively changing the assumed stress–volume material response used in the backward integration such that the stress–time profiles determined from the measurements at each of the sample thicknesses converge, it is possible to obtain a unique stress–volume curve for the material, within the assumptions stated above. Accuracies of a few percent have been quoted for this approach for compressive response over a modest stress range. A notable advantage of the technique is that it exactly corrects for wave perturbations caused by impedance mismatch at free surfaces or sample/window interfaces [41]. The backward analysis technique and the Lagrangian wave analysis method are illustrated in Fig. 1.13a, b.

Forward Analysis Techniques

The backward integration technique and the Lagrangian analysis method are useful for analyzing continuous material response in several different applications. However, both methods have limitations in certain cases. For

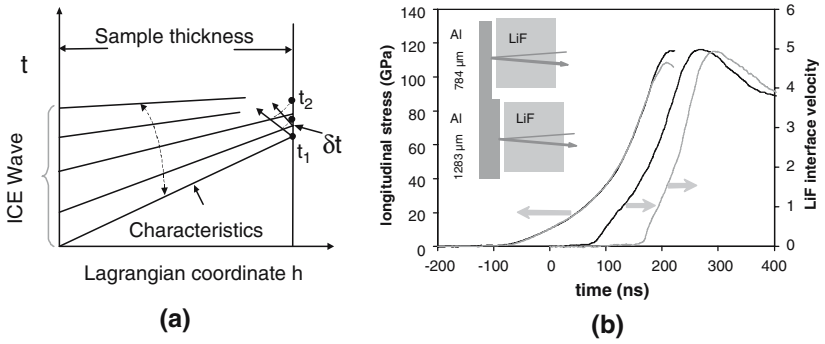

Fig. 1.13. (**a**) Illustration of the affect of wave interactions at an interface. The reflected waves perturb the oncoming compression wave, causing a slight change in the characteristics, resulting in a significant difference in the observed wave profile as compared to the in situ response. (**b**) Backward integration method for determining compression states in ramp loading experiments. The EOS for aluminum is iteratively adjusted until the wave profiles measured from two sample thicknesses (784 and $1,283\,\mu$m) ntegrate back to a common loading profile at $x = 0$. The inferred pressure profiles for the two sample thicknesses differ in peak pressure as a result of wave interactions, which must be carefully considered in analyzing the results. In particular, data above 100 GPa in this experiment are not usable

example, the integration technique is strictly applicable for rate-independent response of fluids where the material flow should be isentropic. The presence of elastic–plastic response in solids with high compressive yield strengths violates this condition and results in nonunique solutions. The Lagrangian analysis technique is powerful for analyzing generalized wave propagation for either rate-independent or rate-dependent response, but it is generally necessary to measure wave profiles at several sample positions to accurately apply the method. Further, the wave profiles should be measured with both stress and particle velocity gauges if possible.

In many material studies, it is not possible to meet either of these requirements. For example, either only a single continuous wave profile can be measured at a specific sample thickness or the compressive material strength of the sample being investigated is extremely high. In these situations, an alternate method of probing material response is attractive and has proven to be quite useful. The technique makes use of measurements of the particle velocity history directly on the drive plate, which is assumed to have a low yield strength, and simultaneously on the back surface of a sample mounted on the drive plate. Using the measured velocity history from the drive plate, the backward integration technique can be used to estimate the input stress history to the plate. Given this stress history, a forward calculation can be performed to model the measured wave profile at the back surface of the

http://www.springer.com/978-3-540-22364-1

Shock Wave Science and Technology Reference Library,
Vol. 2
Solids I
Horie, Y. (Ed.)
2007, XV, 369 p., Hardcover
ISBN: 978-3-540-22364-1